



Plasmonic control of solar-driven CO₂ conversion at the metal/ZnO interfaces



Jiwu Zhao, Bingqian Liu, Lingshu Meng, Sha He, Rusheng Yuan, Yidong Hou, Zhengxin Ding, Huaxiang Lin, Zizhong Zhang, Xuxu Wang, Jinlin Long*

Sate Key Lab of Photocatalysis on Energy and Environment, College of Chemistry, Fuzhou University, Fuzhou, 350116, China

ARTICLE INFO

Keywords:

Surface plasmon resonance
Photocatalysis
CO₂ reduction
Solar hydrocarbon fuels
ZnO nanosheets

ABSTRACT

Molecular-level understanding of the solar-driven CO₂ conversion is of importance to design high-efficiency artificial photosynthetic systems for rebalancing the global carbon cycle. Herein, some physical insights into the surface plasmon resonance (SPR) mediated CO₂ photoreduction were demonstrated with metal (Au, Ag, and Pd)/3D porous ZnO nanosheets (NSs). Such plasmonic photocatalysts were designed elaborately to expose the polar {001} facet, based on the physical prototype of field-field coupling, in order to benefit chemical polarization and activation of the inert molecule. Among these plasmonic metals, gold was found to be not only more effective for promoting the solar-driven CO₂ conversion, but unique for producing the higher hydrocarbon, C₂H₆. A 10-fold enhanced conversion efficiency and a quantum efficiency of 1.03% were achieved on Au/ZnO NSs at ca. 80% selectivity to hydrocarbons under solar light irradiation. The characterization results indicated that the metal-semiconductor interaction enables the electron-phonon decoupling to generate more amounts of energetic electrons in the excited ZnO NSs by a proposed pathway, called the SPR energy transfer induced interband transition that promotes the semiconductor photoexcitation, kinetically accelerating the conversion. Density functional theory calculations revealed that the field-field coupling greatly intensifies the surface polarization for adsorbates, charging negatively the C atom of CO₂ and making O=C=O bond bent, along with the electrophilic attack by two competitive paths, leading to the concomitance of CO and CH₄. The loading of plasmonic metal nanoparticles alters the molecular paths of CO₂ conversion by tuning thermodynamically the first dehydroxylation step, consequently the product selectivity. Especially Au plasmon, it enables the CO hydrogenation path, making CH₄ faster.

1. Introduction

The direct production of renewable hydrocarbon fuels from sunlight, CO₂ and water by artificial photosynthetic systems could provide a scalable grid storage technology for powering the planet [1]. The photocatalyzed conversion of solar-to-hydrocarbon fuels at high efficiency and high product selectivity has thus received intense attention worldwide over the past decades, but advances on the solar fuel technology are still in the proof-of-concept stage [2,3]. The chemical challenges involve mainly both of the adsorption, capture, and activation of atmospheric CO₂ molecules and the complex multielectron transfer processes of CO₂ reduction to an energy-rich fuel or a value-added chemical [4–8], which requires the congregation of electrons and reactive substrates at an active center carrying out the eventual formation of C–H bonds to prevent a wide array of organic products. Therefore, a research goal is to develop an efficient, stable artificial

photosystem that can overcome these limitations and challenges to achieve the efficient conversion of sunlight into hydrocarbons [9–14], especially ethane (C₂H₆) and higher hydrocarbons, by solar-driven CO₂ reduction with H₂O as an electron and proton donor, which is highly desired, and yet formidable in chemistry.

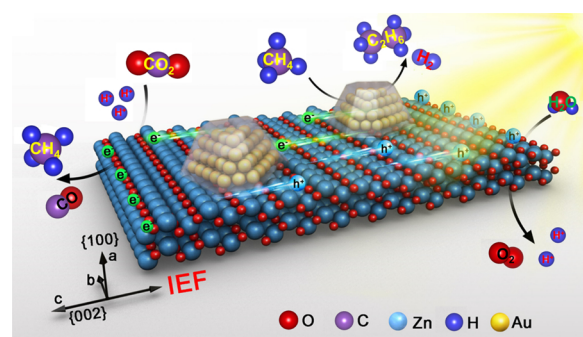
The photochemical conversion of CO₂ to hydrocarbons is a multi-step process. Two possible pathways have been already proposed for the multielectron photocatalysis, depending on whether the hydrogenation path or the deoxygenation path is faster [15–19]. The first step is the CO production, and then CO as an intermediate will be further hydrogenated to CH₄, along the formaldehyde path CO→H₂CO→CH₃OH→CH₄, or the carbene path CO→C[·]→CH₃[·]→CH₃OH/CH₄. The rate-limiting step is the deoxygenation of CO₂ to CO, involving a series of elemental processes including the CO₂ adsorption, the electron transfer, the activation and heterolytic splitting of C=O bonds. The transfer of photoexcited electrons to CO₂ to form the CO₂[–] anion is

* Corresponding Author.

E-mail address: jllong@fzu.edu.cn (J. Long).

most crucial, and yet highly sensitive to the geometry of the adsorbed CO_2 molecule [20–22]. The more bent, the lower the CO_2 LUMO energy, and the easier the electron transfer. This means there are several unique and special requirements for rational design of photocatalysts for the conversion. One is that CO_2 needs a relatively high local electric field, in order to be easily polarized, activated and to allow electrophilic attack, due to the absence of dipole moment, a small polarizability ($29.1 \times 10^{-25} \text{ cm}^3$ for CO_2), and the C=O dissociation energy up to 750 kJ mol^{-1} [23–25]. That is, the chemical affinity of photocatalysts to CO_2 is the principal point. Among those widely-studied oxide photocatalysts (TiO_2 , ZnO , Ga_2O_3 , SrTiO_3 , Zn_2GaO_4 , and Zn_2GeO_4) that can work for the CO_2 photoreduction, wurtzite (hexagonal) structured zinc oxide (ZnO) is eligible to fulfil these unique requirements, because of the strong, spontaneous polarization (0.047 C/m^2) along the $\{001\}$ direction [26,27]. It can induce a non-uniform charge distribution between $[\text{ZnO}]$ layers to form an intrinsic inner electric field (IEF). The IEF not only enables separation of electrons and holes, but also polarizes and activates the unreactive substrate adsorbed on the $\{001\}$ plane [28,29]. Moreover, from the viewpoint of the catalytic reaction kinetics, the conversion can be also prompted by strengthening adsorption of reactive substrates on the surface of semiconductor photocatalysts, reducing the diffusion resistance of reactive substrates, and exposing more amounts of active sites. These kinetics considerations require photocatalysts to be porous, and to expose polar high-energy facets with a strong polarization and heterolytic dissociation of the inert molecule. Therefore, chemically tailoring or modifying the surface and electronic structures at the nanoscale to endow ZnO with distinctive properties is a prerequisite for the CO_2 -to-hydrocarbon conversion at a high product selectivity.

Nevertheless, the CO_2 conversion over photo-excited oxide semiconductors was commonly dominated by the CO evolution ($\text{CO}_2 + 2\text{H}^+ + 2\text{e}^- \rightarrow \text{CO} + \text{H}_2\text{O}$, $E^\circ = -0.53 \text{ V}$ at $\text{pH} = 7.0$, Eq. 1), although it has a more negative reduction potential than the hydrocarbon production ($\text{CO}_2 + 8\text{H}^+ + 8\text{e}^- \rightarrow \text{CH}_4 + 2\text{H}_2\text{O}$, $E^\circ = -0.24 \text{ V}$ at $\text{pH} = 7.0$, Eq. 2; $2\text{CO}_2 + 14\text{H}^+ + 14\text{e}^- \rightarrow \text{C}_2\text{H}_6 + 4\text{H}_2\text{O}$, $E^\circ = -0.27 \text{ V}$ at $\text{pH} = 7.0$, Eq. 3) [30,31]. It implies that the number of electrons trapped at an active site can't afford the eight-electron reduction under irradiation of diffuse solar flux. Utilization of the surface plasmon resonance (SPR) of metallic nanoparticles (NPs) such as Au, Ag, and Pd to concentrate incident photon flux into deep-subwavelength volumes offers a desirable solution to light concentration at the nanometer scale [32–34]. These plasmonic metals can extract and collect photoexcited electrons from the semiconductor across the interfacial Schottky junction. More than this, the loading of these metallic co-catalysts may lower the barrier of CO hydrogenation in virtue of the unique function of hydrogen spillover [35–37], energetically favorable for the formation of C–H bonds. More importantly, some plasmonic metals, for example gold NPs, enable also the direct dissociation of inert C–H bonds by hot electron injection and plasmon-induced resonance energy transfer (PIRET) [29,38,39], exceptionally producing higher hydrocarbons. Taken together, to maximize the efficacy of metallic SPR for the controllable phototransformation of CO_2 to C_2 hydrocarbons, the idealized photocatalysts may possess the unique structural feature as shown in **Scheme 1**. Au nanoparticles (NPs) are dispersedly deposited on the explored nonpolar $\{100\}$ plane of 3D porous ZnO nanosheets (NSs), parallel to the IEF direction. The SPR field parallel to the polar $\{001\}$ facet, coupling with the IEF. The exciton binding energy can be decreased by the field-field coupling, leading to better charge separation, activity, and selectivity under simulated solar light (solar light thereafter) illumination. What's more, based on the catalyst model, the molecular pathways of plasmon-mediated CO_2 photoreduction can be clarified by density functional theory (DFT) calculations. Additionally, other two plasmonic metals (Ag and Pd) were also studied in detail as cocatalysts to gain a comprehensive physical insight into the plasmon-mediated CO_2 conversion at the metal/oxide interfaces.



Scheme 1. Schematic illustration of the idealized Au/ZnO NSs photocatalyst for the CO_2 -to- C_2H_6 conversion.

2. Experimental

2.1. Materials

$\text{Zn}(\text{NO}_3)_2 \cdot 2\text{H}_2\text{O}$, urea ($\text{CO}(\text{NH}_2)_2$), ethylene oxide/propylene oxide block copolymer (F-127), ethanol, chloroauric acid trihydrate ($\text{HAuCl}_4 \cdot 3\text{H}_2\text{O}$), silver nitrate (AgNO_3), and palladium chloride (PdCl_2) were purchased from Sinopharm Chemical Reagent Co. Ltd. All of reagents were of analytical grade and used without any further purification.

2.2. Preparation of $m\text{-ZnO}$ NS arrays

Fluorine-doped tin oxide (FTO) coated glasses ($1 \text{ cm} \times 5 \text{ cm}$) were firstly cleaned by sequential ultra-sonication in isopropanol, acetone, ethanol and deionized water for 1 h and then dried in N_2 stream at room temperature. The conducting side of FTO glass was wetted with zinc acetate ethanol solution (5 mM) for 10 s, dried with N_2 stream, repeating 5 times, and then, annealed at 623 K for 30 min to form a ZnO seed layer.

ZnO NS arrays were synthesized by a modified hydrothermal procedure. Typically, an indicated amount of $\text{Zn}(\text{Ac})_2 \cdot 2\text{H}_2\text{O}$ and $\text{CO}(\text{NH}_2)_2$ was dissolved firstly into deionized water, and then 0.027 g F-127 surfactant was added into the mixed solution of 0.058 M $\text{Zn}(\text{Ac})_2$ and 0.41 M $\text{CO}(\text{NH}_2)_2$, and finally 0.1 mol acetic acid was added to adjust $\text{pH} = 4\text{--}5$ and stirred continuously at the room temperature for 2 h. After the transparent solution was transferred into a dried Teflon-liner stainless steel autoclave with a volume of 100 mL, two pieces of FTO coated with ZnO seed were putted, in which the conducting side was downside. The autoclave was kept at 368 K for 24 h in an electric oven, and then cooled to room temperature. The as-prepared ZnO NS array samples (denoted as $m\text{-ZnO}$) were washed with deionized water and ethanol for several times, dried at 353 K overnight, and finally calcined at 773 K for 10 h.

2.3. Preparation of $M/m\text{-ZnO}$ NS arrays

The $M/m\text{-ZnO}$ NS arrays were prepared by a simple photodeposition method. The as-prepared $m\text{-ZnO}$ NS arrays were immersed into an aqueous solution of $\text{HAuCl}_4 \cdot 3\text{H}_2\text{O}$, AgNO_3 or PdCl_2 , and then irradiated with a Xe lamp to deposit Au, Ag, and Pd NPs onto $m\text{-ZnO}$ NSs for 30 min. The color of $m\text{-ZnO}$ NSs was gradually changed from white to light burgundy. The resultant sample was washed with deionized water and dried at 353 K overnight. The content of metals was regulated by varying the dosage of $\text{HAuCl}_4 \cdot 3\text{H}_2\text{O}$, AgNO_3 or PdCl_2 . The resultant sample was denoted as $M/m\text{-ZnO-}x$, where x stands for the molar percentage of metal content. $M/m\text{-ZnO}$ NSs grown on FTO surface has a ca. 1.0 mg weight.

2.4. Characterizations of M/m-ZnO-x arrays

XRD measurements were performed on a Bruker D8 Advance X-ray diffractometer equipped with a Cu $K_{\alpha 1}$ radiation ($\lambda = 1.5406 \text{ \AA}$). SEM images were taken with a Hitachi S-5800 system. TEM images were obtained by a JEOL model JEM 2010 EX instrument at the accelerating voltage of 200 KV. UV-vis DRS spectra were measured on a Varian Cary 500 Scan UV-vis-NIS spectrophotometer using BaSO₄ as a reference ranging from 200 to 800 nm. XPS data were carried out on an ESCALAB 250 XPS system with a monochromatized Al K α X-ray source (15 KV, 200 W, 500 μm , pass energy = 20 eV). AFM images were recorded using an Agilent 5500 AFM (Agilent Technologies, USA). Raman spectra were obtained at ambient temperature using a Confocal Laser Micro-Raman Spectrometer (inVia-Reflex), and a laser of 532 nm wavelength was used as the light source. The peak fitting of Raman spectra is performed using the Gaussian peak type in the Origin software. The electrochemical analysis including transient photocurrent response and electrochemical impedance spectra were carried out on an epsilon workstation and a ZENNIIUM workstation, respectively. The analysis was performed, respectively, in Na₂SO₄ (0.2 M) and the mixed solution of KCl aqueous solution (0.5 M) and K₃[Fe(CN)₆]/K₄[Fe(CN)₆] (0.01 M) with a ratio of 1:1. ESR signals of the radical spin-trapped by 5, 5-dimethyl-1-pyrroline-N-oxide (DMPO) were examined with a Bruker ESP 300E spectrometer. The freshly prepared DMPO solution (0.2 mol L⁻¹) and suspension of sample (5.0 mg) were mixed directly before their transfer into a cylindrical quartz tube (length 100 mm and diameter 2 mm). The EPR signals of the DMPO-OH, DMPO-O₂^{·-}, and DMPO-[·]CH₂OH spin adducts were detected in water and methanol, respectively. A 300 W commercial Xe lamp was used as a photoexcitation light source, and the ESR spectra were recorded at room temperature. The settings for the EPR spectrometer were as follows: center field, 3510.00 G; microwave frequency, 9.79 GHz; power, 5.05 mW. ESR signals of the photocatalysts were also examined with a Bruker ESP 300E spectrometer. A 300 W commercial Xe lamp was used as a photoexcitation light source, and the ESR spectra were recorded at room temperature. The settings for the EPR spectrometer were as follows: center field, 3510.00 G; microwave frequency, 9.79 GHz; power, 5.05 mW.

2.5. Photocatalytic activity testing

The solar light activities of photocatalytic CO₂ reduction with H₂O was performed in a 40 mL Schlenk flask reactor with a silicone rubber septum under atmospheric pressure and ambient temperature. Loading of the M/m-ZnO NSs photocatalyst uniformly grown on the FTO glass having an area of 5 cm² was 1.0 mg. This system was first evacuated by a mechanical pump and then filled with pure CO₂ gas. The evacuation-filling operation was repeated three times. 1.0 bar of CO₂ and 20 μL of liquid water were introduced finally with a syringe via the septum. A 300 W commercial Xe lamp with a power of 595 mW was used as an irradiation light source and vertically placed outside the reactor. The temperature of the reactor was kept at 298 K with an electronic fan. Every 1 h, 0.5 mL of reactive gas were taken from the reactor with a syringe and analyzed by a GC-7890B gas chromatography equipped with a flame ionized detector (FID), a chromatographic column (GASPRO), and a methane converter.

2.6. DFT calculations

All density functional theory (DFT) calculations were performed by Vienna Ab-initio simulation package (VASP) code [40,41]. The projector-augmented wave (PAW) method was employed to describe the core-valence interactions [42,43], where the cutoff energy of plane wave basis set was 400 eV. The electronic exchange-correlation was treated by the generalized gradient approximation (GGA) with the Perdew-Burke-Ernzerhof (PBE) [44]. In the process of geometry

optimization, the interaction between internal molecules was considered by DFT-D2 method [29]. The force reach convergence accuracy when less than 0.05 eV/Å. According to experimental facts, the simulated structure of catalyst Au/ZnO NSs and Ag/ZnO NSs was modeled with monolayer 7 \times 7 ZnO(001) and bilayer 8 \times 8 Au(111) and Ag (111) supercell, respectively. In addition, taking into account the lattice mismatch, Pd/ZnO NSs was modeled with monolayer 6 \times 6 ZnO(001) and bilayer 7 \times 7 Pd(111). The slab was isolated by a vacuum layer of 20 Å thick and considering the economics of calculation, the Brillouin-zone integration was performed on a special gamma K-points, which can achieve the calculation accuracy [25]. Transition states of elementary reactions were searched by Climbing- nudged elastic band (C-NEB) method [45–47].

The adsorption energy was defined as [47,48]:

$$E_{\text{ads}} = E_{(\text{adsorption state})} - E_{(\text{adsorbate})} - E_{(\text{support})}$$

Where $E_{(\text{adsorption state})}$ is the total energy of the adsorption state involve adsorbate and support, $E_{(\text{adsorbate})}$ and $E_{(\text{support})}$ are the energies of adsorbate in the gas phase and bare support, respectively.

3. Results and discussion

3.1. Preparation and characterizations of M/m-ZnO NSs photocatalysts

A series of the plasmonic photocatalysts, M/m-ZnO-x (M is plasmonic metals including Au, Ag, and Pd, and x denotes the mole percentage of M) were prepared by a modified seed-hydrothermal growth procedure, as depicted in Fig. 1a, where ethylene oxide/propylene oxide block copolymer (denoted as F-127) as a structure-directed template agent and urea were added into the growth solution and FTO glass was used as the substrate [50]. The calcination under flowing O₂ atmosphere at 773 K for 10 h is to completely remove F-127 and other adsorbed carbon sources, which was confirmed by thermogravimetric experiment (Fig. S1). And then metal NPs were in-situ photodeposited on the sintered ZnO NSs under weak acidic conditions with a 300 W Xe lamp irradiation. It can appear from the scanning electron microscope (SEM) image (Fig. 1b) that the bare m-ZnO sample clearly shows micrometer-sized ultrathin nanosheets vertically aligned, uniformly distributed on the whole substrate and formed an intertwined pattern. The X-ray diffraction (XRD) characterization (Fig. S2) clearly indicates that these ZnO NSs have a wurtzite structure (JCPDS No. 36-1451), without any impurity phases. The {100} diffraction peak much stronger than the {002} peak shows the preferred orientation of the nanosheets perpendicular to the c axis. The thickness of the nanosheets is determined to be ca. 1.6 nm by atomic force microscopy (AFM) (Fig. 1c and d), corresponding to six [ZnO] layers along {100} direction. Obviously, the ZnO NSs surface that is normal to the c axis exposes the O, Zn-terminated ZnO {001} planes. The stacking sequences of atomic layers are asymmetric, and thus spontaneously polarized along the c axis (Fig. 1e), generating the intrinsic IEF between Zn-terminated ZnO {001} and O-terminated ZnO {001} planes to more efficiently separate the electron/hole pairs [28,29,51–53], as shown by the 11-fold enhanced photocurrent response of the bare m-ZnO NSs, compared to that of ZnO NRs (Fig. S3). Expectedly, the charge separation efficiency can be enhanced greatly by applying a plasmonic electric field parallel to IEF along the {100} direction. Next, plasmonic metal nanoparticles (NPs) were successfully deposited on the {100} plane by the photochemical protocol. It can be clearly seen from TEM patterns (Fig. 1f and S4) that ZnO NSs are penetrated by a number of irregular pores with a wide diameter size of 10–100 nm, and metal NPs are predominantly deposited on the exposed {100} surface and only a few NPs are placed in pore walls. The metal mean sizes are, respectively, ca. 7.0, 4.0, and 7.0 nm with a narrow distribution at 4.6 mol% loading for Au, at 1.7 mol% loading for Ag, and at 1.9 mol% loading for Pd (Fig. S5), respectively. The high-resolution TEM (HRTEM) image (Fig. 1g–i) exhibits an interplanar

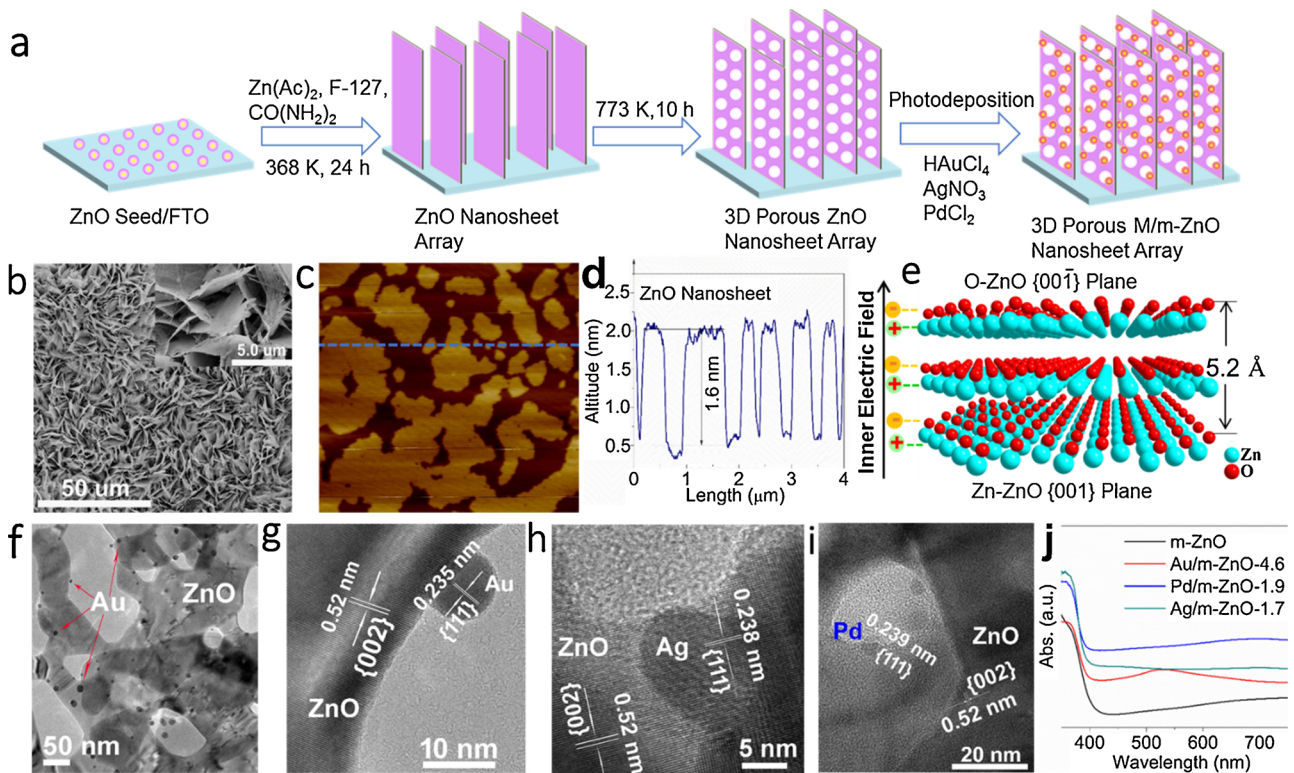
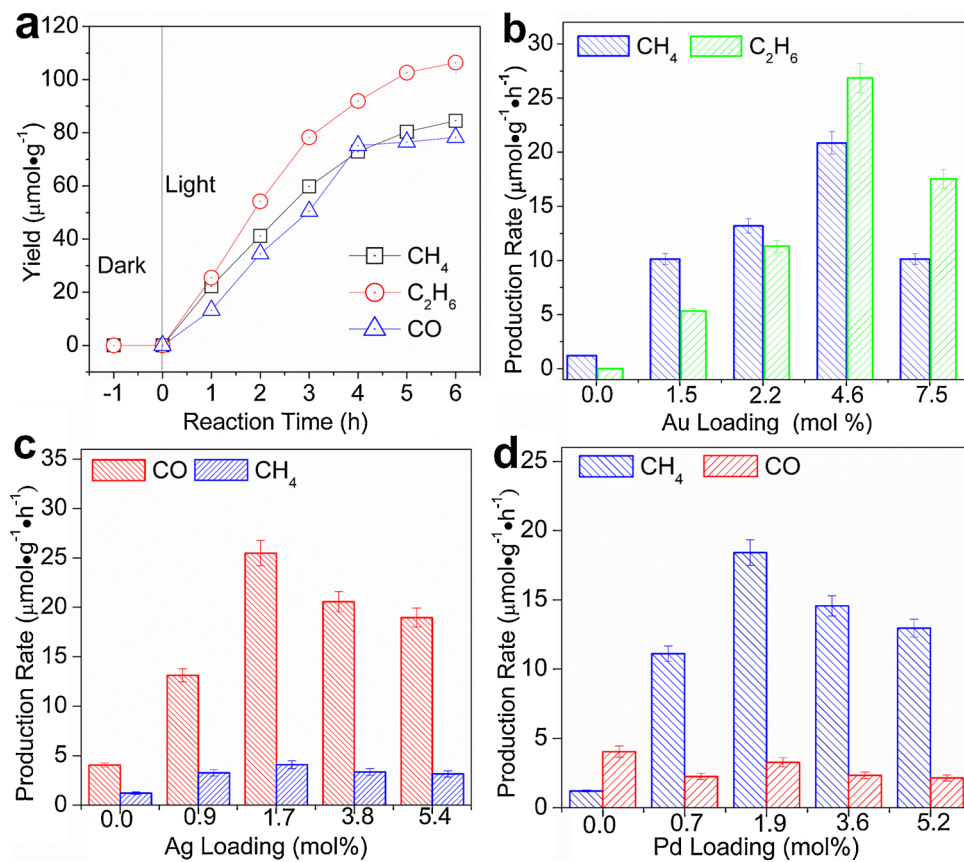


Fig. 1. Design, structural and optical characterizations of plasmonic metal/m-ZnO-x NSs arrays. (a) schematic preparation procedure of plasmonic metal/m-ZnO-x NSs arrays, (b) SEM image of 3D porous ZnO NSs array, (c) AFM image of 3D porous ZnO NSs, (d) AFM Height profile of 3D porous ZnO NSs, (e) crystal structure and charge distribution of ZnO NSs along the {001} facet, (f) TEM image of Au/m-ZnO-4.6 sample, (g) HRTEM image of Au/m-ZnO-4.6 sample, (h) HRTEM image of Ag/m-ZnO-1.7 sample, (i) HRTEM image of Pd/m-ZnO-1.9 sample, (j) UV-vis diffuse reflection spectra of m-ZnO, Au/m-ZnO-4.6, Ag/m-ZnO-1.7, and Pd/m-ZnO-1.9 samples, where the pronounced broad absorption above 500 nm originates from the optical interfere inside the nanosheets array [49].

spacing of ca.0.24 nm corresponding to the {111} crystal plane of face-centered cubic (fcc) metals (0.235 nm for Au, 0.238 nm for Ag, and 0.239 nm for Pd) and an interplanar spacing of 0.52 nm indexed to the {002} direction of ZnO NSs. The photodeposition of these metal NPs does not alter the shape, size, and crystal phase of these ZnO NSs (Fig. S2). When the metal molar percentage is more than 4.6% for Au, 1.7% for Ag, and 3.6% for Pd, two typical diffraction peaks indexed to the {111} and {200} facets of fcc-phase metals (JCPDS 04-0784) appears, indicating the formation of metallic Au, Ag, Pd NPs. All the samples show a band-gap absorption at ca. 395 nm, corresponding to the band-gap energy of 3.14 eV (Fig. 1j). The photodeposition of metal NPs does not change the intrinsic band-edge absorption of ZnO NSs, but generates a long tail absorption broadened to the near infrared (NIR) region (Fig. S6). The intensity of tail absorption increases with metal loading, improving drastically the solar light utilization. Different from the Pd, Ag-loaded samples, the Au/m-ZnO-x samples show clearly an optical absorption band centered at 530 nm, belonging to the SPR band of Au NPs. The plasmonic absorptions of Ag and Pd NPs in the Ag/m-ZnO-x and Pd/m-ZnO-x samples were entirely damped, even indiscernible due to the interfacial strong-interaction. It was well established that the interfacial damping of plasmons can aid the injection of hot electrons from metal NPs to the conduction band of ZnO NSs [54–56], and yet the quick recombination at a *ps* lifetime limits greatly the chemical action of plasmonic hot charges, especially for the multi-electron photocatalysis. More attention will be paid to the plasmon resonance energy transfer (PRET), which is able to improve greatly the rate of optical energy absorption of the semiconductor and enhance the electric field intensity in a small, well-defined location of the semiconductor.

3.2. Solar photocatalytic conversion of CO₂ to hydrocarbons

The photocatalytic performance of these M/m-ZnO-x NSs array samples for the CO₂-to-hydrocarbon conversion was tested under simulated sunlight ($\lambda > 320$ nm, solar light thereafter) illumination, as shown in Fig. 2a representing the evolution of products, CO, CH₄ and C₂H₆, obtained using the representative Au/m-ZnO-4.6 photocatalyst. Upon light irradiation, the yields of CO, CH₄ and C₂H₆ increase with irradiation time. Several control activity results (Table S2) further indicate that the conversion is indeed triggered by light excitation of the photocatalyst. For the bare m-ZnO NSs (Fig. 2b), CO is predominant, and yet methane is the only hydrocarbon product. The Au photodeposition significantly enhances the photocatalytic efficiency of the m-ZnO NSs array. More surprisingly, a large amount of C₂H₆ is generated, besides CH₄. The optimal CO₂ conversion is achieved at an Au loading of 4.6 mol%, which shows the highest evolution rates of CH₄ (21.0 $\mu\text{mol g}^{-1} \text{h}^{-1}$) and C₂H₆ (27.0 $\mu\text{mol g}^{-1} \text{h}^{-1}$). More Au NP loading (> 4.6 mol%) results in a decrease in the production rates of CH₄ and C₂H₆ because of the stronger photon scattering and the competitive photon absorption between Au NPs and ZnO NSs in the UV region of 200–400 nm [57]. The total carbon yield reaches up to ca. 75 $\mu\text{mol g}^{-1} \text{h}^{-1}$ at 4.6 mol% Au loading (Fig. 2b) and reached a quantum efficiency of 1.03% (Fig. S7). Interestingly, two reference samples, Au/ZnO-NRs and Au/ZnO-NPs where Au NPs were deposited on the polar {001} facet (Fig. S8), only produce CO and CH₄, and no C₂H₆ was detected by GC (Fig. S9). This clearly indicates that the C₂H₆ evolution is related closely to the coupling of SPR field with IEF field. However, the loading of Ag and Pd NPs showed a different product distribution for the conversion (Fig. 2c and d), without C₂H₆ evolution. CO is predominantly generated on the Ag/m-ZnO-x photocatalysts, and yet the Pd/m-ZnO-x photocatalysts mainly convert CO₂ into CH₄, along with a small amount of CO. The highest CO production rate



($25.0 \mu\text{mol g}^{-1} \text{h}^{-1}$) is achieved on Ag/m-ZnO-1.7, and the highest CH_4 evolution rate is $18.0 \mu\text{mol g}^{-1} \text{h}^{-1}$ with Pd/m-ZnO-1.9. Evidently, the activity results of M/m-ZnO-x photocatalysts are not corresponding to their optical absorptions. As shown in Fig. S6, the absorption intensity monotonously increases with metal loading, without maximum in the visible region. Such a discrepancy is mainly originated from the stronger light harvesting of the plasmonic metals for solar electromagnetic spectrum compared to the polar ZnO absorber. The activity results indicate conclusively that the photo-excited metals contributed to the tremendous improvement of solar-driven CO_2 conversion on ZnO NSs.

The more important attention should be paid to the product selectivity for the photocatalytic conversion of CO_2 to hydrocarbons. Commonly, CO_2 is photocatalytically converted into CO on the bare metal oxides, along with a minor amount of CH_4 [58–61]. Surprisingly, Au or Pd loading changes the product selectivity and greatly enhances the hydrocarbon production, while Ag is more positive for the CO production. It can be seen from Fig. 3a that for the Au loading, the hydrocarbon yield is ca. 10-fold enhanced at 4.6 mol%, and the selectivity of the main product, C_2H_6 , is parallel to the Au loading. It is monotonously increased to ca. 65% at 7.5 mol % of Au NPs, while the CH_4 selectivity is reduced reversely. This implies that CH_4 is further converted into C_2H_6 . Our previous study showed that Au NPs enable the dehydrogenative coupling of methane to ethane and hydrogen on the polar ZnO NSs [29]. Ag loading increases the CO selectivity from 77% to 86% at 1.7 mol%, corresponding to the decrease of CH_4 selectivity from 23% to 14% (Fig. 3b). Pd loading accelerates the methane evolution. The CH_4 selectivity increases sharply and reaches to 85% at 1.9 mol%, corresponding to the decrease of CO selectivity from 77% to 15%. All samples are photocatalytically stable for the conversion. As shown in Fig. 3d–f, after running recycle of 4–6 times, the production rate of main products is relatively constant on Au/m-ZnO-4.6, Ag/m-ZnO-1.7 and Pd/m-ZnO-1.9. The enormous change in product

selectivity maybe results from the strong metal-semiconductor interaction, which alters the molecular pathway of CO_2 conversion. It will be confirmed by DFT calculations later.

3.3. The thermodynamic analysis of CO_2 -to-Hydrocarbons conversion with DFT calculations

The thermodynamic analysis of CO_2 -to-hydrocarbons conversion with DFT calculations. To understand in depth the origin on product selectivity and to reveal in the molecular level the conversion pathway, we used density function theory (DFT) to calculate in detail the potential energy diagram of the CO_2 conversion on the 2D structure cells of $\text{Zn}_{49}\text{O}_{49}$ monolayer, $\text{Zn}_{49}\text{O}_{49}/\text{Au}_{128}(111)$, $\text{Zn}_{49}\text{O}_{49}/\text{Ag}_{128}(111)$, and $\text{Zn}_{36}\text{O}_{36}/\text{Pd}_{98}(111)$, extracted from the polar $\text{Zn}(001)$ surface. All of intermediates and steps involving in six possible conversion paths, were considered because the CO_2 conversion undergoes the hydrogenation on either the C atom or the O atoms via the proton-coupled electron transfer processes (Eqs. 1 and 2). It is thus reasonable in our calculations that hydrogens are assumed to be added one by one to CO_2 , as indicated in Fig. 4. The hydrogenation on the C atom of CO_2 has four possible paths, $\text{CO}_2 \rightarrow \text{H}_2\text{COOH}^* \rightarrow \text{H}_2\text{CO}^* \rightarrow \text{H}_3\text{COH}^* \rightarrow \text{H}_3\text{C}^* \rightarrow \text{CH}_4$ (P1), $\text{CO}_2 \rightarrow \text{H}_3\text{COOH}^* \rightarrow \text{H}_3\text{CO}^* \rightarrow \text{H}_3\text{COH}^* \rightarrow \text{H}_3\text{COH}^* \rightarrow \text{H}_4\text{COH}^* \rightarrow \text{CH}_4$ (P2), $\text{CO}_2 \rightarrow \text{H}_3\text{COOH}^* \rightarrow \text{H}_3\text{CO}^* \rightarrow \text{H}_3\text{COH}^* \rightarrow \text{H}_3\text{C}^* \rightarrow \text{CH}_4$ (P3), and $\text{CO}_2 \rightarrow \text{H}_2\text{COOH}^* \rightarrow \text{H}_2\text{CO}^* \rightarrow \text{H}_3\text{COH}^* \rightarrow \text{H}_4\text{COH}^* \rightarrow \text{CH}_4$ (P4). The difference among them lies in the two dehydroxylation steps. The paths of $\text{CO}_2 \rightarrow \text{COOH}^* \rightarrow \text{CO} \rightarrow \text{H}_2\text{CO}^* \rightarrow \text{H}_4\text{COH}^* \rightarrow \text{CH}_4$ (P5) and $\text{CO}_2 \rightarrow \text{COOH}^* \rightarrow \text{CO} \rightarrow \text{H}_2\text{CO}^* \rightarrow \text{H}_3\text{C}^* \rightarrow \text{CH}_4$ (P6) are the cross-hydrogenation on O and C atoms and have a difference in the second dehydroxylation process. CO is generated by the (P5) and (P6) paths. The potential energy diagrams of all of CO_2 -to- CH_4 conversion paths were calculated and showed in Fig. 5. It can appear that when CO_2 is adsorbed alone on the polar $\text{Zn}(001)$ surface of bare ZnO NSs and M/ZnO NSs, as expected, the adsorption is spontaneous, and slightly stronger on Au/ZnO NSs and Pd/ZnO NSs with an adsorption energy of ca. -0.20 eV

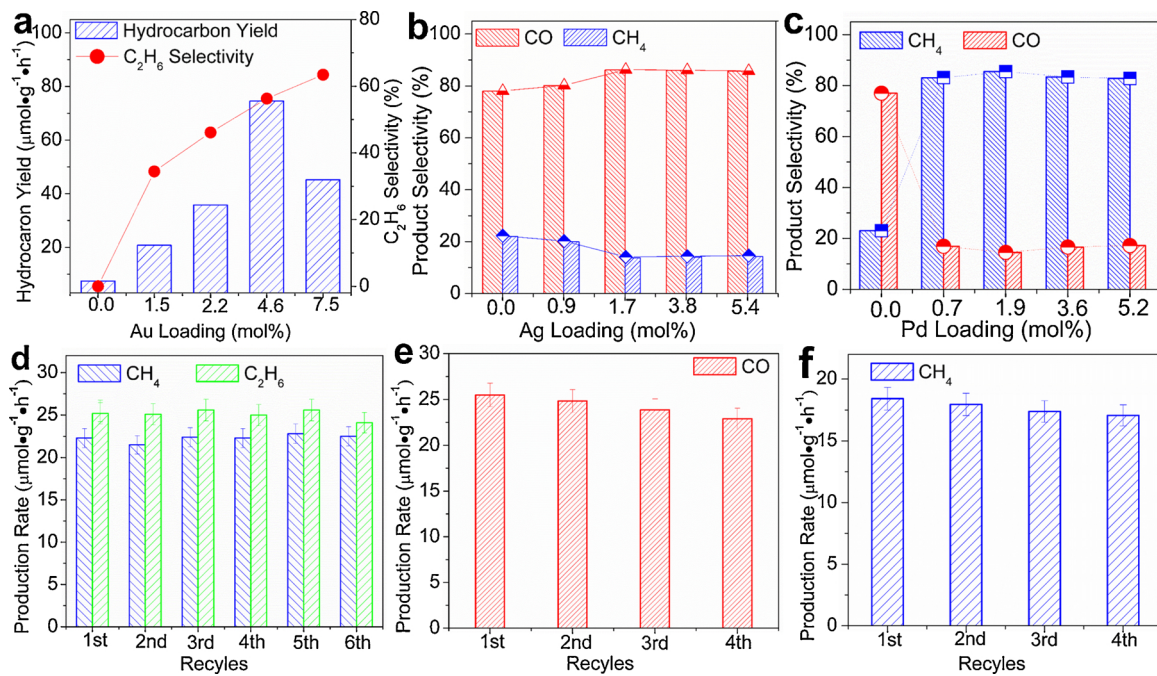


Fig. 3. Product selectivity and activity stability for the Solar-driven CO₂ conversion. (a) Hydrocarbon yield and C₂H₆ selectivity function as Au loading, (b) product selectivity functions as Ag loading, (c) product selectivity functions as Pd loading, (d) activity stability over the Au/m-ZnO-4.6 array, (e) activity stability over the Ag/m-ZnO-1.7 array, (f) activity stability over the Pd/m-ZnO-1.9 array.

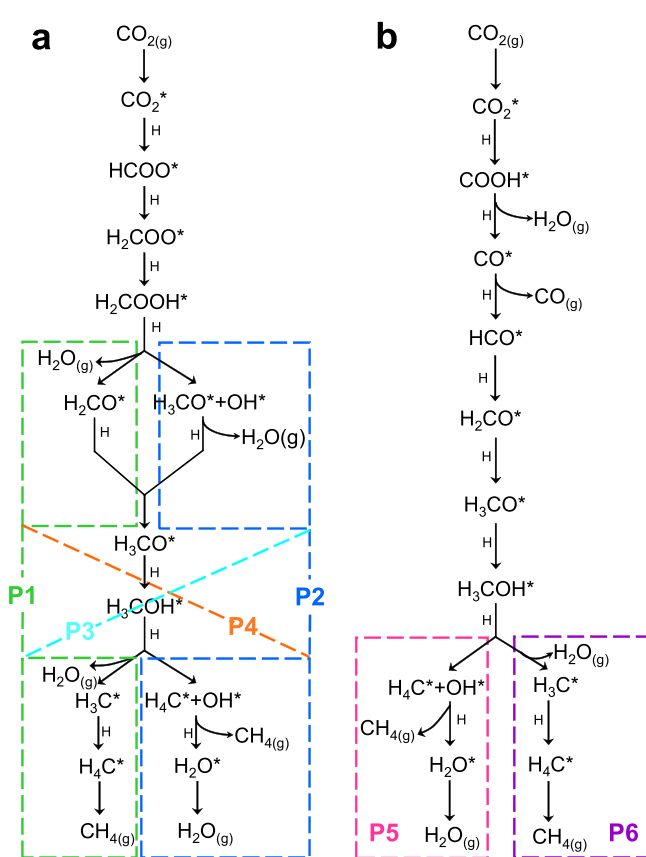


Fig. 4. Six possible hydrogenation pathways for the CO₂-to-CH₄ conversion. (a) The hydrogenation on the C atom of CO₂; (b) the cross-hydrogenation on the O and C atoms.

compared to bare ZnO NSs (-0.18 eV) and Ag/ZnO NSs (-0.12 eV). The optimized geometries, corresponding structural parameters and adsorption energies are given in Fig. S10 and Table S2 (See supporting information materials). It can be justified from the average length of nascent O-Zn bonds that the binding strength of CO₂ follows the order of Au/ZnO NSs > Ag/ZnO NSs > Pd/ZnO NSs > bare ZnO NSs. As sketched in Fig. S10-b, g, i and q, CO₂ can be chemoadsorbed stably in the form of bidentate species on the Zn(001) plane, and yet a different adsorption mode occurs between after and before loading of Au and Ag NPs. The optimized configuration of Z-L shows a linear adsorption state with a C–O bond length of 1.18 Å essentially equal to the corresponding gaseous value, and a nascent O–Zn bond with an average length of ca. 3.2 Å. The \angle O–C–O bonding angle is shrunk slightly by 0.2°. It indicates clearly that CO₂ is physisorbed on the Zn (001) plane of bare ZnO NSs. Pd NPs can strengthen the physisorbsorption (PdZ-L2, see supporting information materials), while they are inactive for promoting the chemical polarization of CO₂ on the Zn(001) surface. After loading Pd NPs, the \angle O–C–O bonding angle is shrunk from 179.8° to 179.2° and the average length of O–Zn bonds is decreased from 3.2 Å to 3.0 Å. Surprisingly, in the presence of Au and Ag, the CO₂ adsorption is changed completely, occurring in a M configuration. The two optimized configurations of AuZ-B1 and AgZ-B1 are highly similar to the S1 excited state structure with a C–O bond of 1.21 \pm 0.01 Å [62]. CO₂ bridges a low coordinated Zn–O dimer via two C=O bonds, thus creating two nascent O–Zn bonds with an average length of ca. 2.30 Å. The surface molecule is visibly deformed compared to its gaseous counterpart, with the internal C=O bonds elongated to an average length of 1.21 \pm 0.01 Å. It can be seen from Table S2 that the \angle O–C–O bonding angle is shrunk from 180.0° to 145.0° on Au/ZnO NSs, and to 148.5° on Ag/ZnO NSs. It indicates conclusively that Au and Ag NPs greatly intensify the surface polarization for the adsorbate, making the O=C=O bond bent and negatively charging it. The enhanced polarization is an indicative of the field-field coupling, which is confirmed experimentally by the CO₂-TPD results of Au/ZnO NSs showed in Fig. S11, and yet Pd is one exception. The field-field coupling charges negatively the ZnO NSs, as shown in Fig. S12. The local electron density of the ZnO

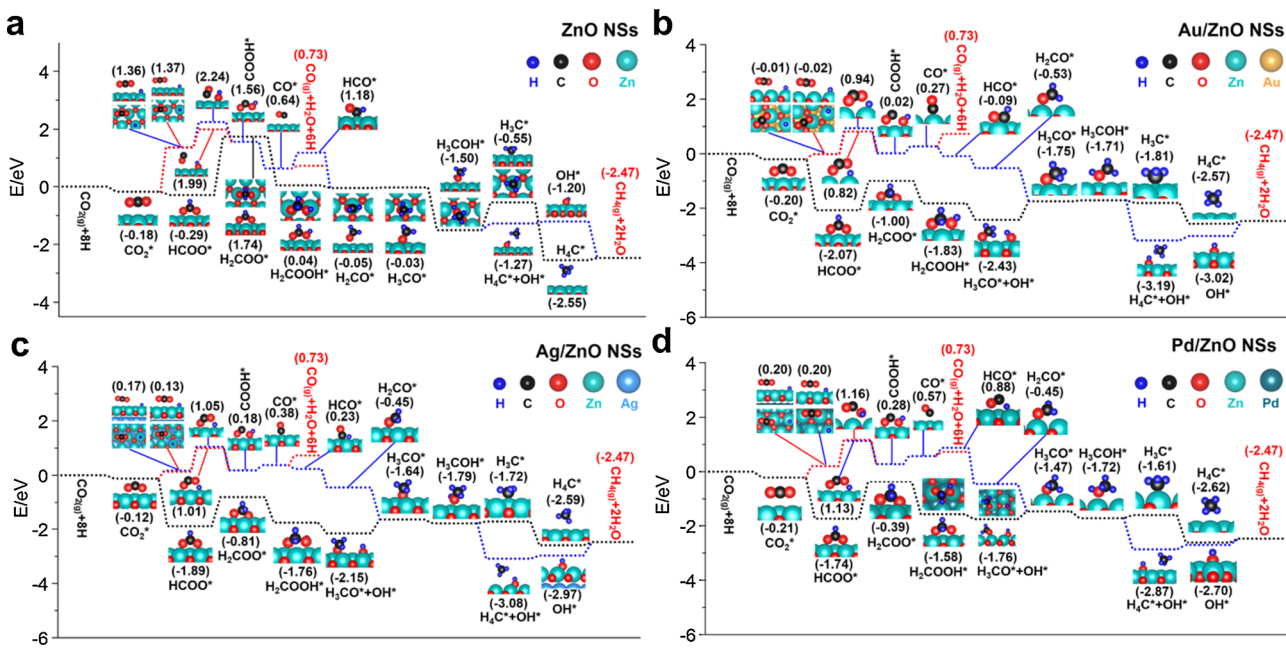


Fig. 5. Potential energy diagram for the CO_2 -to- CH_4 reaction on (a) $\text{Zn}_{49}\text{O}_{49}$, (b) $\text{Zn}_{49}\text{O}_{49}/\text{Au}_{128}(111)$, (c) $\text{Zn}_{49}\text{O}_{49}/\text{Ag}_{128}(111)$, and (d) $\text{Zn}_{36}\text{O}_{36}/\text{Pd}_{98}(111)$ (energy in eV).

moiety is increased at the interface of Au/ZnO NSs and Ag/ZnO NSs (Fig. S12-a, b) by the electron transfer from metals to the ZnO monolayer, showing that the contribution of the field-field coupling to charge flow and separation is larger than that of the Schottky-junction that drives conversely electrons from the semiconductor to Au and Ag NPs. But on the Pd/ZnO NSs, the Schottky-junction formed at the interface of Pd/ZnO NSs is predominant, consequently increasing the electron density of interfacial Pd atoms (Fig. S12-c). Both of the XPS results (Fig. S13) and the Mott-Schottky analysis (Fig. S14) further confirmed the calculated results. After adsorption of CO_2 , the electric field-driven charge transfer from catalyst to adsorbate is more visible for Au/ZnO NSs, where the electrons are delocalized spatially on a larger scale compared to Ag/ZnO NSs and Pd/ZnO NSs, following the order of Au/ZnO NSs > Ag/ZnO NSs > Pd/ZnO NSs.

When CO_2 and H were co-adsorbed, as shown in Fig. 5 and Table S3. There exists three co-adsorption states, depended on the adsorption site of hydrogen that is pivotal to determine the reaction paths. when hydrogen is adsorbed at 1 Zn-site (Fig. S10-a, f, k and p), it is immediately transferred into the C atom of CO_2 to form a new C–H bond, releasing the adsorption heats of -0.29 eV on bare ZnO NSs, -2.07 eV on Au/ZnO NSs, -1.89 eV on Ag/ZnO NSs, and -1.74 eV on Pd/ZnO NSs, respectively (Fig. 5). The P1-4 hydrogenation paths can be started by a stable HCO_2^* intermediate bonded to two Zn sites ($\text{CO}_2^* + \text{H} \rightarrow \text{HCO}_2^*$, Eq. 4). The optimized configurations of Z-B1, AuZ-B1, AgZ-B1, and PdZ-B1 (Fig. S10-c, h, m and r) show that the intermediate has a C–H bond length of ca. 1.12 ± 0.01 Å and a shorter O–Zn bond with a length of 2.10 ± 0.05 Å. Evidently, the loading of metals decreases the adsorption energy by an order of magnitude, thermodynamically feasible to the first step of hydrogenation path. However, there is a large barrier as high as $+2.03$ eV for the second step of the hydrogenation path ($\text{HCO}_2^* + \text{H} \rightarrow \text{H}_2\text{CO}_2^*$, Eq. 5) on the bare ZnO NSs (Fig. 5a). At the dehydroxylation step of H_3COH^* to CH_4 , there are two possibilities. H is added on the C atom to form CH_4 with a low barrier of $+0.22$ eV, and yet the barrier increased to $+0.95$ eV upon addition of H on O atom. Evidently, the elemental reaction of $\text{H}_3\text{COH}^* + \text{H} \rightarrow \text{CH}_4 + \text{OH}^*$ (Eq. 6) is more thermodynamically preferential, consequently excluding the paths of P1, P3, and P6. In addition, it was found that at the H_2COOH^* hydrogenation step, H is added to the OH group of H_2COOH^* to form H_2CO^* and H_2O , which is a thermodynamic feasible process with an exothermic energy of -0.01 eV ($\text{H}_2\text{COOH}^* + \text{H} \rightarrow \text{H}_2\text{CO}^* + \text{H}_2\text{O}$, Eq.

7). The elemental reaction of $\text{H}_2\text{COOH}^* + \text{H} \rightarrow \text{H}_3\text{COOH}^*$ (Eq. 8) does not occurs on bare ZnO NSs. It can be therefore concluded that the conversion of CO_2 to CH_4 on bare ZnO NSs follows the P4 path. Surprisingly, the thermodynamic barriers of the two dehydroxylation steps (Eqs. 4 and 6) can be reduced drastically by the metal/oxide interaction. It appears from Fig. 5b-d that the former (Eq. 4) decreases from $+2.03$ eV to $+1.07$ eV for Au/ZnO NSs, to $+1.08$ eV for Ag/ZnO NSs, and to $+1.35$ eV for Pd/ZnO NSs, and the latter (Eq. 6) decreases from $+0.25$ eV to -1.48 eV for Au/ZnO NSs, to -1.29 eV for Ag/ZnO NSs, and to -1.15 eV for Pd/ZnO NSs. The result indicates that the Eq. 6 reaction goes spontaneously on M/ZnO NSs, forming CH_4 . It can well explain the photocatalytic activity result that no CH_3OH is detected. Another one path, $\text{H}_3\text{COH}^* + \text{H} \rightarrow \text{H}_3\text{C}^* + \text{H}_2\text{O}$ (Eq. 9), is not a priority to the CH_4 formation on M/ZnO NSs, but feasible due to the low thermodynamic barrier. Unexpectedly, the H_2CO^* formation by the Eq. 7 reaction became to be thermodynamic infeasible, while the Eq. 8 reaction occurs with an exothermic energy of -0.60 eV for Au/ZnO NSs, -0.39 eV for Ag/ZnO NSs and -0.18 eV for Pd/ZnO NSs. A new rate-controlled step occurs at the dehydroxylation process of $\text{H}_3\text{COOH}^* + \text{H} \rightarrow \text{H}_3\text{CO}^* + \text{H}_2\text{O}$ (Eq. 10), the calculated heat of which follows the order of Au/ZnO NSs ($+0.68$ eV) > Ag/ZnO NSs ($+0.51$ eV) > Pd/ZnO NSs ($+0.29$ eV). The conversion of CO_2 to CH_4 on m/ZnO NSs follows preferentially the P2 path. It can be therefore concluded that the loading of metal NPs alters the molecular pathway of the CO_2 -to- CH_4 conversion on the Zn(001) plane of ZnO NSs, via the metal-semiconductor interaction.

Interestingly, when H was co-adsorbed at 2 or 3 Zn-sites, the deoxygenation of $\text{CO}_2 \rightarrow \text{CO}$, is started across a transition state (TS), as depicted in Fig. 5. For bare ZnO NSs and Pd/ZnO NSs, there is lack of change in the bonding configuration of the adsorbate. However, on Au/ZnO NSs and Ag/ZnO NSs, the chemoadsorption of CO_2 is altered into the physisorption. The optimized configurations of Z-L2, Z-L3, AuZ-L2, AuZ-L3, AgZ-L2, AgZ-L3, PdZ-L2, and PdZ-L3 (Fig. S10-d, e, i, j, n, o, s and t) display that the bent CO_2 molecule is back to be linear. The O–Zn bond length is elongated from 2.30 ± 0.05 Å to 3.00 ± 0.05 Å, and the C–O bond length is shortened from 1.21 ± 0.01 Å to 1.18 ± 0.01 Å. The endothermic energies of $+1.36$ – 1.37 eV implies that the co-adsorption is very difficult on bare ZnO NSs, corresponding to the poor photocatalytic activity. The loading of metal cocatalysts

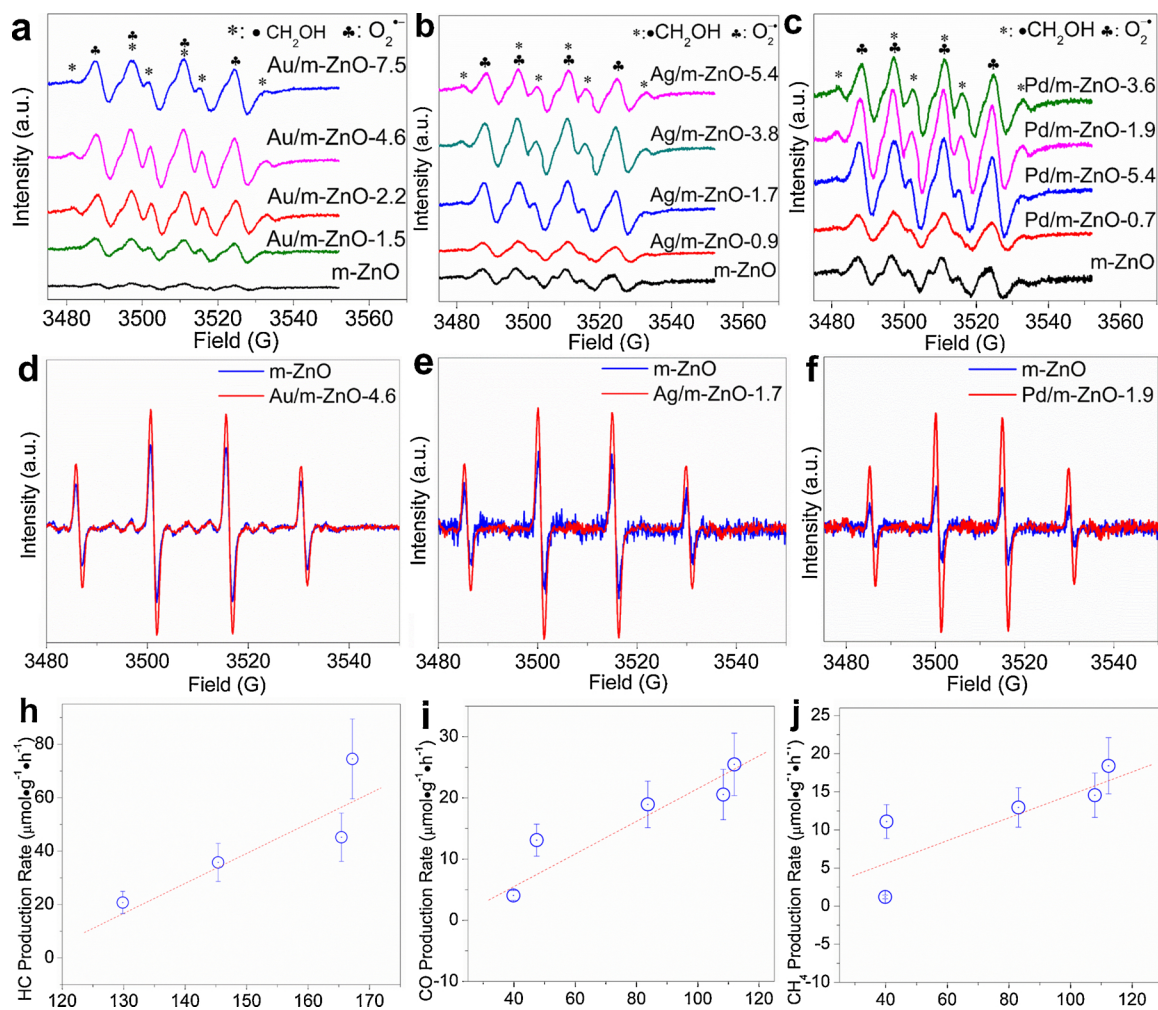


Fig. 6. Spin trapping EPR spectra at 298 K of DMPO-O₂⁻ (a-c) and DMPO-·OH (d-f) adducts generated on the m-ZnO and M/m-ZnO-x photocatalysts with solar light excitation. Correlation between the photogenerated electrons and the main production rates on (h) Au/m-ZnO-x, (i) Ag/m-ZnO-x, and (j) Pd/m-ZnO-x. Four characteristic signals belonging to the DMPO-·OH adduct appear in Fig. 6d-f, indicating the formation of ·OH radicals by the hole oxidation of water (H₂O + h⁺ → ·OH + H⁺, E = + 2.72 eV, Eq. 14) [65].

greatly reduces the co-adsorption energy. The decrease follows the order of Au/ZnO NSs (1.39 eV) > Ag/ZnO NSs (1.20 eV) > Pd/ZnO NSs (1.17 eV), coincident with the enhanced conversion. Not badly, the activation energy of the elementary step of CO₂^{*} + H → COOH^{*} (Eq. 11) increases slightly by 0.2-0.3 eV. But the exothermic dehydroxylation step of COOH^{*} + H → CO^{*} + H₂O (Eq. 12) is reversed to be endothermic, where the calculated adsorption enthalpies (ΔH) are equal to + 0.25 eV on Au/ZnO NSs, to + 0.20 eV on Ag/ZnO NSs, to + 0.29 eV on Pd/ZnO NSs. It indicates clearly that the presence of metal cocatalysts is thermodynamically unfavorable to the dehydroxylation. Comparison of the desorption energy and hydrogenation energy of CO on catalysts finds that the latter is smaller than the former on both of bare ZnO NSs and Pd/ZnO NSs, indicating the priority of CO desorption to the further hydrogenation conversion of CO^{*} + H → HCO^{*} (Eq. 13). On both of Au/ZnO NSs and Ag/ZnO NSs, the latter is larger than the former. However, the competition of the desorption with the hydrogenation is inclined to the latter on Au/ZnO NSs, and yet the former on Ag/ZnO NSs, bare ZnO NSs and Pd/ZnO NSs. This is mainly because the formation enthalpy (ΔH = - 0.36 eV) of the hydrogenation reaction (Eq. 13) on Au/ZnO NSs is more negative than those of Ag/ZnO NSs (ΔH = - 0.15 eV), bare ZnO NSs (ΔH = + 0.54 eV) and Pd/ZnO NSs (ΔH = + 0.33 eV). The CO intermediate can be partly hydrogenated to finally form CH₄ by the P5 path on Au/ZnO NS. As a result, the CO evolution rate on Au/ZnO NSs (ca. 13 μmol g⁻¹ h⁻¹) is lower than that of Ag/ZnO

NSs (ca. 24 μmol g⁻¹ h⁻¹). It can well explain the activity result that the CO evolution rate follows the order of Ag/m-ZnO-1.7 > Au/m-ZnO-4.6 > m-ZnO NSs > Pd/m-ZnO-1.9. These results imply that the hydrogenation of CO to H₂CO is kinetically controlled. Although it is a spontaneous process on Ag/ZnO NSs, a faint amount of the CO intermediate can be further hydrogenated to CH₄, as indicated by the minor enhancement of the CH₄ evolution rate in Fig. 2c. The dehydroxylation is the rate-controlled step for the CO production in the P5 path. It can well explain the fact that CO can be always detected in the CO₂ photoreduction reported in literature [63,64].

In a word, the CO₂ photoreduction follows two competitive paths, leading to the concomitance of CO and CH₄. Loading of metal cocatalysts is not only positive for reducing the thermodynamic barrier of the CO₂-to-CH₄ conversion paths on ZnO NSs, but alters the molecular pathways of the solar-driven CO₂ conversion. The DFT results show clearly that the dehydroxylation from COOH^{*} and H₂COOH^{*} is the most pivotal rate-controlled step determining which one path is faster. The product selectivity is tunable by balancing the kinetics and thermodynamics of the rate-controlled step. Among M/ZnO NSs, Pd/ZnO NSs show the lowest thermodynamic barrier (+ 0.29 eV) of the dehydroxylation from H₂COOH^{*} and the highest thermodynamic barrier (+ 0.29 eV) of the dehydroxylation from COOH^{*}, explaining the extraordinary selectivity to CH₄ on the Pd-supported photocatalysts. Ag/ZnO NSs give the lowest thermodynamic barrier (+ 0.2 eV) of the

dehydroxylation from COOH^* , beneficial to CO production. Moreover, the CO desorption is kinetically preferential to its further hydrogenation on Ag/ZnO NSs, suppressing the CH_4 formation. Au NPs show its specificity for improving the solar-driven CO_2 conversion in the following two aspects: One is that they can further convert CH_4 into C_2H_6 on the $\text{Zn}(001)$ plane of ZnO NSs by the dehydrogenative coupling mechanism, as showed in our previous work [29]. Another is that they enable the hydrogenation of CO to CH_4 by the P5 path, making CH_4 faster. Compared to bare ZnO NSs, M/m-ZnO NSs shows the significantly-enhanced yields of CO and CH_4 . It implies that the local electron density of active sites at the interface of photoexcited M/ZnO NSs increases by the metal/semiconductor interaction.

3.4. The strong interaction of SPR field with free electrons for enhancing band-gap excitation

To understand the physical fundamental of metal-semiconductor interaction. Spin trap electron paramagnetic resonance (EPR) spectroscopy was used to determine the amount of electrons photogenerated on the m-ZnO NSs by the elementary reaction of $\text{O}_2 + \text{e}^- \rightarrow \text{O}_2^-$ [66]. DMPO was used to trap the active free radicals formed upon light on. As showed in Fig. 6a–c, the several characteristic EPR signals assigned to the DMPO- O_2^- and DMPO- $\cdot\text{CH}_2\text{OH}$ adducts indicate the formation of O_2^- and $\cdot\text{CH}_2\text{OH}$ radicals. The DMPO- $\cdot\text{CH}_2\text{OH}$ adduct is originated from the hole oxidation of methanol [67]. The EPR lines of the O_2^- radical are very weak for the ultrathin m-ZnO NSs, while the photo-deposition of metal NPs on the surface of ZnO NSs results in the formation of more amounts of O_2^- radical. The EPR signals are significantly intensified with metal loadings. Compared to the m-ZnO NSs, the EPR signal intensity of the DMPO- O_2^- adduct increases by several folds, even an order of magnitude on these M/m-ZnO-x photocatalysts. The signal intensity reaches a maxima at $x = 4.6$ for Au, at $x = 1.7$ for Ag, and at $x = 1.9$ for Pd, perfectly corresponding to the activity of the CO_2 photo-reduction. Furthermore, comparison of the EPR spectra of the DMPO- $\cdot\text{OH}$ adduct generated on bare m-ZnO NSs and M/m-ZnO NSs (Fig. 6d–f) finds that the loading of plasmonic metals enables the significant enhancement of holes photogenerated on ZnO NSs. A near linear correlation between the intensity of DMPO- O_2^- signal versus the evolution rate of main products is established (Fig. 6h–j), further confirming that the plasmon-enhanced CO_2 -to- CH_4 conversion follows the photocatalytic mechanism of energetic electrons-induced reduction by the proton-coupled electron transfer process (Eq. (2)).

To further verify the EPR results, we performed the photoelectrochemical characterization of several representative photocatalysts including bare m-ZnO, Au/m-ZnO-4.6, Ag/m-ZnO-1.7, and Pd/m-ZnO-1.9 to determine the formation and separation of energetic electrons. Fig. 7 a–c show the periodic on/off photocurrent response of such catalysts when irradiated under intermittent solar light sunlight. Solar light irradiation of bare m-ZnO NSs grown on fluorine-doped indium tin oxide (FTO) glass reveals a relatively low short-circuit photocurrent, whereas the loadings of Au, Ag and Pd NPs result in, respectively, a 8-fold, 2-fold, and 7-fold increase in the photocurrent. The multiplicative photocurrents are originated from the co-excitation of plasmonic metal NPs and ZnO NSs under solar light irradiation. Visible light excitation of plasmonic metal NPs produce energetic “hot” electrons, which can inject in part into m-ZnO NSs, but its efficiency is well-known to be as low as 0.1% [68–73] that the contribution of plasmonic “hot” electrons to the multiplicative photocurrents is minor, even negligible [74–78]. Although the fact that the d-band electrons of metal NPs can be excited to form energetic “hot” electrons by the high energy UV photons cannot be ignored⁵, the low loading limits the UV-photon harvesting capability. As depicted in Fig. 7d–f, there is a threshold photon energy for the d-band excitation, which is estimated by $E = E_p + \Phi_b$, where E_p and Φ_b are the plasmonic absorption energy and the Schottky barrier, respectively. It is calculated that the threshold energy for Au, Ag, and Pd NPs is equal to 3.3, 3.54 and 3.23 eV, respectively. It is positioned at the

intrinsic optical absorption region of ZnO NSs, close to its band gap dominated by excitonic effects (Fig. 1j). But the competition for the light-harvesting is inclined to ZnO NSs due to the larger mass ratio of ZnO NSs to metal NPs. Moreover, the probability of energetic d-band electron transfer from the photoexcited metal NPs to the semiconductor is extremely small because the conduction band position of the photo-excited semiconductor is shifted towards more positive energy. Therefore, it can be concluded that the SPR-enhanced band-gap excitation maybe contributes predominantly to the tremendous increase in photogenerated electrons and holes by decreasing the electron-phonon coupling strength and Coulomb carrier-carrier interaction in the polar ZnO NSs.

To confirm the above-mentioned conclusion, resonance Raman spectroscopy was used to estimate the coupling strength of electron and longitudinal optical (LO) phonons in ZnO NSs after and before the loading of plasmonic metal NPs [79–81]. Fig. S15 (see supporting information) shows the typical Raman spectra of ZnO NSs. All observed vibrational modes in ZnO NSs, both first order and second order scattering, were assigned on the basis of group theoretical analysis and given in Table S4 (see supporting information). It can appear that several peaks centered at 331, 379, 437, 542, 585, and 661 cm^{-1} are observed in the low wavenumber region on the Raman spectrum of ZnO NSs. In the large wavenumber region of $700\text{--}1300\text{ cm}^{-1}$, three broadened peaks located, respectively, at 987, 1105, and 1155 cm^{-1} are also found. After loading plasmonic metal NPs, several changes are clearly discernible. One is that the smooth spectrum of ZnO NSs becomes rough owing to the SPR-enhanced Raman scattering. Importantly, the two phonon modes at 1105 and 1155 cm^{-1} , which are assigned, respectively, to the combination of A1 and E2 Raman bands and the second order overtone band of A1, shift significantly towards the low-wavenumber region. As shown in Fig. S14b, the red shift is huge for the Au-deposited ZnO NSs and follows the order of Au/m-ZnO-4.6 > Ag/m-ZnO-1.7 > Pd/m-ZnO-1.9, suggesting that the second order LO phonons of ZnO NSs were spatially confined at the M/ZnO interface, depended on the metal-semiconductor interaction strength (Au/ZnO NS > Ag/ZnO NSs > Pd/ZnO NSs). The electron-LO-phonon coupling strength was determined by the ratio of second-to-first order Raman scattering cross sections. As show in Fig. S14c, compared to the bare ZnO NSs, the loading of plasmonic metal NPs leads to a significant decrease in the ratio of 2LO to 1LO, indicating that the SPR field is able to reduce the Fröhlich interaction between charged carriers and long-range dipole field of these LO phonons in ZnO NSs.

Finally, based on the above-mentioned experimental and analysis results, the physical mechanism of plasmon-enhanced solar CO_2 conversion is clearly revealed, as schemed in Fig. 7d–f. The injection of plasmonic hot electrons and d-band electrons from photoexcited metal NPs contributed minor to the enhancement of photocatalytic activities and photocurrents. It is originated mainly from the SPR-enhanced band-gap excitation. Under solar light illumination, the SPR field enables the electron-phonon decoupling in the UV-light excited ZnO NSs by the PRET pathway, making the electrons placed on the conduction band bottom of ZnO NSs transited to higher energy levels. The occurrence of interband transition can increase greatly the band-gap photoexcitation, as a result, the more energetic electrons facilitate kinetically the CO_2 conversion, associated closely with the metal/semiconductor interaction strength.

4. Conclusions

In summary, a 10-fold-enhanced efficiency of solar-to-hydrocarbon conversion at an impressive selectivity to ethane was achieved by depositing Au NPs on the {100} facets of 3D porous ZnO NSs with a thickness of ca. 1.6 nm. The molecular pathways and rate-controlled steps of the plasmon-mediated CO_2 conversion were clarified fully by DFT calculations. It was well established that the loading of plasmonic metal NPs, especially Au, is not only able to intensify the chemical

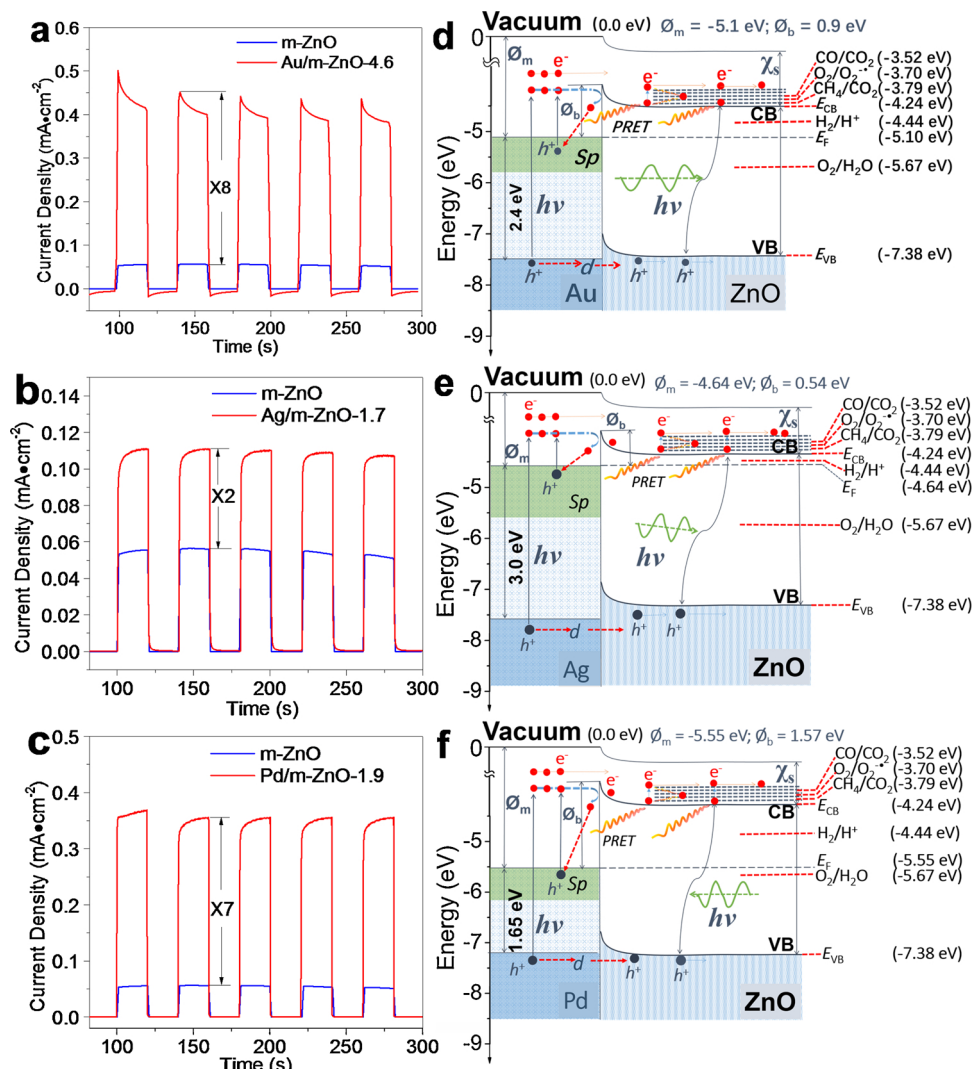


Fig. 7. Short-circuit photocurrent response of Au/m-ZnO-4.6 (a), Ag/m-ZnO-1.7 (b) and Pd/m-ZnO-1.9 (c) photocatalysts in a 0.2 M Na_2SO_4 aqueous electrolyte with intermittent solar light irradiation. The schematic physical mechanism of plasmon-enhanced solar CO_2 conversion on M/ZnO catalysts. (d) Au/m-ZnO NS. (e) Ag/m-ZnO NS. (f) Pd/m-ZnO NS.

polarization and activation of the inert molecule, but tunes thermodynamically the dehydroxylation step, which is the rate-limiting step, by the metal/semiconductor interaction, changing the molecular paths of CO_2 conversion. A pathway, called the SPR energy transfer-induced interband transition (SPRETIT), was proposed to reasonably elucidate the plasmon-enhanced CO_2 conversion. The characterization results showed that the field-field coupling is able to reduce the Fröhlich interaction, generating more amounts of energetic electrons by the SPRETIT mechanism. This work shows the last advance in the plasmonic photocatalysis for solar carbon fuel production, also contributes to not only some novel insights into the plasmon-mediated CO_2 conversion, but also a smart strategy to design of high efficient photocatalysts for the chemical conversion of unreactive small molecules.

Author contributions

J. Long conceived the concept, directed the research and wrote the paper. J. Zhao, B. Liu, L. Meng, and S. He. carried out the catalyst preparation and the activity experiments. R. Yuan, Y. Hou, Z. Ding and H. Lin. performed the EPR experiments. Z. Zhang and X. Wang revised the manuscript. All authors discussed the results and reviewed the manuscript.

Declaration of interest

The authors declare no competing financial interests.

Acknowledgment

This work was financially supported by the NSFC (Grants No. 21773031 and U1805255), the Natural Science Foundation of Fujian Province of P. R. China (2018J01686), and the State Key Laboratory of Photocatalysis on Energy and Environment (SKLPEE-2017A01 and SKLPEE-2017B02).

Appendix A. Supplementary data

Supplementary material related to this article can be found, in the online version, at doi:<https://doi.org/10.1016/j.apcath.2019.117823>.

References

- [1] N.S. Lewis, D.G. Nocera, Powering the planet: chemical challenges in solar energy utilization, *Proc. Natl. Acad. Sci. U. S. A.* 103 (2006) 15729–15735, <https://doi.org/10.1073/pnas.0603395103>.
- [2] N.S. Lewis, Research opportunities to advance solar energy utilization, *Science* 351 (2016) 1920, <https://doi.org/10.1126/science.ad1920>.

[3] C. Liu, B.C. Colón, M. Ziesack, P.A. Silver, D.G. Nocera, Water splitting-biosynthetic system with CO₂ reduction efficiencies exceeding photosynthesis, *Science* 352 (2016) 1210–1213, <https://doi.org/10.1126/science.aaf5039>.

[4] J. Long, H. Chang, Q. Gu, J. Xu, L. Fan, S. Wang, Y. Zhou, W. Wei, L. Huang, X. Wang, P. Liu, W. Huang, Gold-plasmon enhanced solar-to-hydrogen conversion on the {001} facets of anatase TiO₂ nanosheets, *Energy Environ. Sci.* 7 (2014) 973–977, <https://doi.org/10.1039/C3EE43289K>.

[5] W. Hou, W.H. Hung, P. Pavaskar, A. Goepert, M. Aykol, S.B. Cronin, Photocatalytic conversion of CO₂ to hydrocarbon fuels via plasmon-enhanced absorption and metallic interband transitions, *ACS Catal.* 1 (2011) 929–936, <https://doi.org/10.1021/cs2001434>.

[6] G. Zeng, J. Qiu, Z. Li, P. Pavaskar, S.B. Cronin, CO₂ Reduction to Methanol on TiO₂-Passivated GaP Photocatalysts, *ACS Catal.* 4 (2014) 3512–3516, <https://doi.org/10.1021/cs500697w>.

[7] G. Chen, R. Gao, Y. Zhao, Z. Li, G.I.N. Waterhouse, R. Shi, J. Zhao, M. Zhang, L. Shang, G. Sheng, X. Zhang, X. Wen, L.-Z. Wu, C.-H. Tung, T. Zhang, Alumina-supported CoFe alloy catalysts derived from layered-double-hydroxide nanosheets for efficient photothermal CO₂ hydrogenation to hydrocarbons, *Adv. Mater.* 30 (2018) 1704663, <https://doi.org/10.1002/adma.201704663>.

[8] Y. Zhao, G. Chen, T. Bian, C. Zhou, G.I.N. Waterhouse, L.-Z. Wu, C.-H. Tung, L.J. Smith, D. O'Hare, T. Zhang, Defect-rich ultrathin ZnAl-layered double hydroxide nanosheets for efficient photoreduction of CO₂ to CO with water, *Adv. Mater.* 27 (2015) 7824–7831, <https://doi.org/10.1002/adma.201503730>.

[9] H. Zhao, X. Ding, B. Zhang, Y. Li, C. Wang, Enhanced photocatalytic hydrogen evolution along with byproducts suppressing over Z-scheme Cd_xZn_{1-x}S/Au/g-C₃N₄ photocatalysts under visible light, *Sci. Bull.* 62 (2017) 602–609, <https://doi.org/10.1016/j.scib.2017.03.005>.

[10] R. Shi, Y. Cao, Y. Bao, Y. Zhao, G.I.N. Waterhouse, Z. Fang, L.-Z. Wu, C.-H. Tung, Y. Yin, T. Zhang, Self-assembled Au/CdSe nanocrystal clusters for plasmon-mediated photocatalytic hydrogen evolution, *Adv. Mater.* 29 (2017) 1700803, <https://doi.org/10.1002/adma.201700803>.

[11] H. Huang, J. Lin, G. Zhu, Y. Weng, X. Wang, X. Fu, J. Long, A long-lived mono-nuclear cyclopentadienyl ruthenium complex grafted onto anatase TiO₂ for efficient CO₂ photoreduction, *Angew. Chem. Int. Ed.* 55 (2016) 8314–8318, <https://doi.org/10.1002/anie.201602796>.

[12] A. Ge, P.E. Videla, B. Rudshteyn, Q. Liu, V.S. Batista, T. Lian, Dopant-dependent SFG response of rhodium CO₂ reduction catalysts chemisorbed on SrTiO₃ (100) single crystals, *J. Phys. Chem. C* 122 (2018) 13944–13952, <https://doi.org/10.1021/acs.jpcc.8b01123>.

[13] C.L. Anfuso, R.C. Snoeberger, A.M. Ricks, W. Liu, D. Xiao, V.S. Batista, T. Lian, Covalent attachment of a rhodium bipyridyl CO₂ reduction catalyst to rutile TiO₂, *J. Am. Chem. Soc.* 133 (2011) 6922–6925, <https://doi.org/10.1021/ja2013664>.

[14] M.L. Clark, A. Ge, P.E. Videla, B. Rudshteyn, C.J. Miller, J. Song, V.S. Batista, T. Lian, C.P. Kubiak, CO₂ reduction catalysts on gold electrode surfaces influenced by large electric fields, *J. Am. Chem. Soc.* 140 (2018) 17643–17655, <https://doi.org/10.1021/jacs.8b09852>.

[15] L. Liu, F. Fan, Z. Jiang, X. Gao, J. Wei, T. Fang, Mechanistic study of Pd–Cu bimetallic catalysts for methanol synthesis from CO₂ hydrogenation, *J. Phys. Chem. C* 121 (2017) 26287–26299, <https://doi.org/10.1021/acs.jpcc.7b06166>.

[16] G. Kumari, X. Zhang, D. Devasia, J. Heo, P.K. Jain, Watching visible light-driven CO₂ reduction on a plasmonic nanoparticle catalyst, *ACS Nano* 12 (2018) 8330–8340, <https://doi.org/10.1021/acsnano.8b03617>.

[17] Y.F. Zhao, R.J. Rousseau, J. Li, D. Mei, Theoretical study of syngas hydrogenation to methanol on the polar Zn-Terminated ZnO(0001) surface, *J. Phys. Chem. C* 116 (2012) 15952–15961, <https://doi.org/10.1021/jp211055s>.

[18] S. Liu, Y.W. Li, J. Wang, H. Jiao, Reactions of CO, H₂O, CO₂, and H₂ on the clean and precovered Fe(110) Surfaces – A DFT investigation, *J. Phys. Chem. C* 119 (2015) 28377–28388, <https://doi.org/10.1021/acs.jpcc.5b07497>.

[19] H.V. Thang, S. Tosoni, G. Pacchioni, Evidence of charge transfer to atomic and molecular Adsorbates on ZnO/X(111) (X = Cu, Ag, Au) ultrathin films. Relevance for Cu/ZnO catalysts, *ACS Catal.* 8 (2018) 4110–4119, <https://doi.org/10.1021/acscatal.7b03896>.

[20] X. Nie, X. Jiang, H. Wang, W. Luo, M.J. Janik, Y. Chen, X. Guo, C. Song, Mechanistic understanding of alloy effect and water promotion for Pd–Cu bimetallic catalysts in CO₂ hydrogenation to methanol, *ACS Catal.* 8 (2018) 4873–4892, <https://doi.org/10.1021/acscatal.7b04150>.

[21] S. Kattel, P. Liu, J.G. Chen, Tuning selectivity of CO₂ hydrogenation reactions at the metal/oxide interface, *J. Am. Chem. Soc.* 139 (2017) 9739–9754, <https://doi.org/10.1021/jacs.7b05362>.

[22] S. Chu, P. Ou, P. Ghamari, S. Vanka, B. Zhou, I. Shih, J. Song, Z. Mi, Photoelectrochemical CO₂ reduction into syngas with the metal/oxide interface, *J. Am. Chem. Soc.* 140 (2018) 7869–7877, <https://doi.org/10.1021/jacs.8b03067>.

[23] S. Yu, A.J. Wilson, J. Heo, P.K. Jain, Plasmonic control of multi-electron transfer and C–C coupling in visible-light-driven CO₂ reduction on Au nanoparticles, *Nano Lett.* 18 (2018) 2189–2194, <https://doi.org/10.1021/acs.nanolett.7b05410>.

[24] S. Xie, Q. Zhang, G. Liu, Y. Wang, Photocatalytic and photoelectrocatalytic reduction of CO₂ using heterogeneous catalysts with controlled nanostructures, *Chem. Commun.* 47 (2016) 35–59, <https://doi.org/10.1039/C5CC07613G>.

[25] P. Rallapalli, K.P. Prasanth, D. Patil, R.S. Somani, R.V. Jasra, H.C. Bajaj, Sorption studies of CO₂, CH₄, N₂, CO, O₂ and Ar on nanoporous aluminum terephthalate [MIL-53(A)], *J. Porous Mater.* 18 (2011) 205–210, <https://doi.org/10.1007/s10934-010-9371-7>.

[26] B. Zhang, Z. Wang, B. Huang, X. Zhang, X. Qin, H. Li, Y. Dai, Y. Li, Anisotropic photoelectrochemical (PEC) performances of ZnO single-crystalline photoanode: effect of internal electrostatic fields on the separation of photogenerated charge carriers during PEC water splitting, *Chem. Mater.* 28 (2016) 6613–6620, <https://doi.org/10.1021/acs.chemmater.6b02639>.

[27] Y. Chen, H. Zhao, B. Liu, H. Yang, Charge separation between wurtzite ZnO polar {0 0 1} surfaces and their enhanced photocatalytic activity, *Appl. Catal. B: Environ.* 163 (2015) 189–197, <https://doi.org/10.1016/j.apcatb.2014.07.044>.

[28] Z. Zhan, Y. Wang, Z. Lin, J. Zhang, F. Huang, Study of interface electric field affecting the photocatalysis of ZnO, *Chem. Commun.* 47 (2011) 4517–4519, <https://doi.org/10.1039/C1CC10888C>.

[29] L. Meng, Z. Chen, Z. Ma, S. He, Y. Hou, H.-H. Li, R. Yuan, X.-H. Huang, X. Wang, X. Wang, J. Long, Gold plasmon-induced photocatalytic dehydrogenative coupling of methane to ethane on polar oxide surfaces, *Energy Environ. Sci.* 11 (2018) 294–298, <https://doi.org/10.1039/C7EE02951A>.

[30] J.L. White, M.F. Baruch, J.E. Pander, Y. Hu, I.C. Fortmeyer, J.E. Park, T. Zhang, K. Liao, J. Gu, Y. Yan, T.W. Shaw, E. Abelev, A.B. Bocarsly, Light-driven heterogeneous reduction of carbon dioxide: photocatalysts and photoelectrodes, *Chem. Rev.* 115 (2015) 12888–12935, <https://doi.org/10.1021/acs.chemrev.5b00370>.

[31] X. Chang, T. Wang, J. Gong, CO₂ photo-reduction: insights into CO₂ activation and reaction on surfaces of photocatalysts, *Energy Environ. Sci.* 9 (2016) 2177–2196, <https://doi.org/10.1039/C6EE00383D>.

[32] J.A. Schuller, E.S. Barnard, W. Cai, Y.C. Jun, J.S. White, M.L. Brongersma, Plasmonics for extreme light concentration and manipulation, *Nat. Mater.* 9 (2010) 193–204, <https://doi.org/10.1038/nmat2630>.

[33] P.-Y. Chen, X. Dang, M.T. Klug, J. Qi, N.M. Dorval Courchesne, F.J. Burpo, N. Fang, P.T. Hammond, A.M. Belcher, Versatile three-dimensional virus-based template for dye-sensitized solar cells with improved Electron transport and light harvesting, *ACS Nano* 7 (2013) 6563–6574, <https://doi.org/10.1021/nn4014164>.

[34] P. Kolchin, N. Pholchai, M.H. Mikkelsen, J. Oh, S. Ota, M.S. Islam, X. Yin, X. Zhang, High purcell factor due to coupling of a single emitter to a dielectric slot waveguide, *Nano Lett.* 15 (2015) 464–468, <https://doi.org/10.1021/nl5037808>.

[35] R. Prins, Hydrogen spillover. Facts and fiction, *Chem. Rev.* 112 (2012) 2714–2738, <https://doi.org/10.1021/cr200346z>.

[36] S.K. Beaumont, S. Alayoglu, C. Specht, N. Kruse, G.A. Somorjai, A nanoscale demonstration of hydrogen atom spillover and surface diffusion across silica using the kinetics of CO₂ methanation catalyzed on spatially separate Pt and Co nanoparticles, *Nano Lett.* 14 (2014) 4792–4796, <https://doi.org/10.1021/nl501969k>.

[37] B.T. Loveless, C. Buda, M. Neurock, E. Iglesias, CO chemisorption and dissociation at high coverages during CO hydrogenation on Ru catalysts, *J. Am. Chem. Soc.* 135 (2013) 6107–6121, <https://doi.org/10.1021/ja311848e>.

[38] X.C. Ma, Y. Dai, L. Yu, B.B. Huang, Energy transfer in plasmonic photocatalytic composites, *Light Sci. Appl.* 5 (2016) e16017, , <https://doi.org/10.1038/lsa.2016.17>.

[39] M.L. Brongersma, N.J. Halas, P. Nordlander, Plasmon-induced hot carrier science and technology, *Nat. Nanotech.* 10 (2015) 25–34, <https://doi.org/10.1038/nnano.2014.311>.

[40] G. Kresse, J. Furthmüller, Efficient iterative schemes for ab initio total-energy calculations using a plane-wave basis set, *Phys. Rev. B* 54 (1996) 11169–11186, <https://doi.org/10.1103/PhysRevB.54.11169>.

[41] G. Kresse, J. Furthmüller, Efficiency of ab-initio total energy calculations for metals and semiconductors using a plane-wave basis set, *Comp. Mater. Sci.* 6 (1996) 15–50, [https://doi.org/10.1016/0927-0256\(96\)00008-0](https://doi.org/10.1016/0927-0256(96)00008-0).

[42] G. Kresse, D. Joubert, From ultrasoft pseudopotentials to the projector augmented-wave method, *Phys. Rev. B* 59 (1999) 1758–1775, <https://doi.org/10.1103/PhysRevB.59.1758>.

[43] P.E. Blöchl, Projector augmented-wave method, *Phys. Rev. B* 50 (1994) 17953–17979, <https://doi.org/10.1103/PhysRevB.50.17953>.

[44] J.P. Perdew, K. Burke, M. Ernzerhof, Generalized gradient approximation made simple, *Phys. Rev. Lett.* 77 (1996), <https://doi.org/10.1103/PhysRevLett.77.3865>.

[45] G. Henkelman, H. Jónsson, A generalized solid-state nudged elastic band method, *J. Chem. Phys.* 113 (2000) 9978–9985, <https://doi.org/10.1063/1.3684549>.

[46] G. Henkelman, B.P. Uberuaga, H. Jónsson, A climbing image nudged elastic band method for finding saddle points and minimum energy paths, *J. Chem. Phys.* 113 (2000) 9901–9904, <https://doi.org/10.1063/1.1329672>.

[47] X. Cui, J. Wang, B. Liu, S. Ling, R. Long, Y. Xiong, Turning Au nanoclusters catalytically active for visible-light-driven CO₂ reduction through bridging ligands, *J. Am. Chem. Soc.* 140 (2018) 16514–16520, <https://doi.org/10.1021/jacs.8b06723>.

[48] B. Liu, Z. Zhao, G. Henkelman, W. Song, Computational design of a CeO₂-supported Pd-based bimetallic nanorod for CO oxidation, *J. Phys. Chem. C* 120 (2016) 5557–5564, <https://doi.org/10.1021/acs.jpcc.6b00253>.

[49] A. Dabirian, R.V.D. Krol, High-temperature ammonolysis of thin film Ta₂O₅ photoanodes: evolution of structural, optical, and photoelectrochemical properties, *Chem. Mater.* 27 (2015) 708–715, <https://doi.org/10.1021/cm503215p>.

[50] H. Zhang, R. Wu, Z. Chen, G. Liu, Z. Zhang, Z. Jiao, Self-assembly fabrication of 3D flower-like ZnO hierarchical nanostructures and their gas sensing properties, *CrystEngComm* 14 (2012) 1775–1782, <https://doi.org/10.1039/C1CE06163A>.

[51] Y. Zhang, Y. Zhang, L. Song, Y. Su, Y. Guo, L. Wu, T. Zhang, Illustration of charge transfer in graphene-coated hexagonal ZnO photocatalysts using Kelvin probe force microscopy, *RSC Adv.* 8 (2018) 885–894, <https://doi.org/10.1039/C7RA12037K>.

[52] J. Li, H. Li, G. Zhan, L. Zhang, Solar water splitting and nitrogen fixation with layered bismuth oxyhalides, *Acc. Chem. Res.* 50 (2017) 112–121, <https://doi.org/10.1021/acs.accounts.6b00523>.

[53] T.-J. Liu, Q. Wang, P. Jiang, Morphology-dependent photo-catalysis of bare zinc oxide nanocrystals, *RSC Adv.* 3 (2013) 12662–12670, <https://doi.org/10.1039/C3RA41399C>.

[54] M.A. Garcia, J. de la Venta, P. Crespo, J. LLopis, S. Penadés, A. Fernández, A. Hernando, Surface plasmon resonance of capped Au nanoparticles, *Phys. Rev. B* 72 (2005) 241403, , <https://doi.org/10.1103/PhysRevB.72.241403>.

[55] M. Liu, P. Guyot-Sionnest, Synthesis and optical characterization of Au/Ag core/

shell nanorods, *J. Phys. Chem. B* 108 (2004) 5882–5888, <https://doi.org/10.1021/jp037644o>.

[56] L. Ochoo, C. Migwi, J. Okumu, Damping effect of the inner band electrons on the optical absorption and bandwidth of metal nanoparticles, *J. Nanopart. Res.* 14 (2012) 1261, <https://doi.org/10.1007/s11051-012-1261-2>.

[57] L. Suljo, C. Phillip, D.B. Ingram, Plasmonic–metal nanostructures for efficient conversion of solar to chemical energy, *Nat. Mater.* 10 (2011) 911–921, <https://doi.org/10.1038/nmat3151>.

[58] T.W. Woollerton, S. Sheard, E. Reisner, E. Pierce, S.W. Ragsdale, F.A. Armstrong, Efficient and clean photoreduction of CO₂ to CO by enzyme-modified TiO₂ nanoparticles using visible light, *J. Am. Chem. Soc.* 132 (2010) 2132–2133, <https://doi.org/10.1021/ja910091z>.

[59] K. Teramura, T. Tanaka, H. Ishikawa, Y. Kohno, T. Funabiki, Photocatalytic reduction of CO₂ to CO in the presence of H₂ or CH₄ as a reductant over MgO, *J. Phys. Chem. B* 108 (2004) 346–354, <https://doi.org/10.1021/jp0362943>.

[60] J.L. Dimeglio, R. Joel, Selective conversion of CO₂ to CO with high efficiency using an inexpensive bismuth-based electrocatalyst, *J. Am. Chem. Soc.* 135 (2013) 8798–8801, <https://doi.org/10.1021/ja4033549>.

[61] A.R. Brian, A. Salehi-Khojin, M.R. Thorsen, W. Zhu, D.T. Whipple, P.J.A. Kenis, R.I. Masel, Ionic liquid–mediated selective conversion of CO₂ to CO at low overpotentials, *Science* 334 (2011) 643–644, <https://doi.org/10.1126/science.1209786>.

[62] W. Taifan, J.F. Boily, J. Baltrusaitis, Surface chemistry of carbon dioxide revisited, *Surf. Sci. Rep.* 71 (2016) 595–671, <https://doi.org/10.1016/j.surfrept.2016.09.001>.

[63] W.N. Wang, W.-J. An, B. Ramalingam, S. Mukherjee, D.M. Niedzwiedzki, S. Gangopadhyay, P. Biswas, Size and structure matter: enhanced CO₂ photo-reduction efficiency by size-resolved ultrafine Pt nanoparticles on TiO₂ single crystals, *J. Am. Chem. Soc.* 134 (2012) 11276–11281, <https://doi.org/10.1021/ja304075b>.

[64] F. Fresno, P. Reñones, E. Alfonso, C. Guillén, J.F. Trigo, J. Herrero, L. Collado, V.A. De la Peña O’Shea, influence of surface density on the CO₂ photoreduction activity of a DC magnetron sputtered TiO₂ catalyst, *Appl. Catal. B: Environ.* 224 (2018) 912–918, <https://doi.org/10.1016/j.apcatb.2017.11.022>.

[65] J. Long, S. Wang, H. Chang, B. Zhao, B. Liu, Y. Zhou, W. Wei, X. Wang, L. Huang, W. Huang, Bi₂MoO₆ Nanobelts for Crystal Facet-Enhanced Photocatalysis, *Small* 10 (2014) 2791–2795, <https://doi.org/10.1002/smll.201302950>.

[66] C. Chen, W. Ma, J. Zhao, Semiconductor-mediated photodegradation of pollutants under visible-light irradiation, *Chem. Soc. Rev.* 39 (2010) 4206–4219, <https://doi.org/10.1039/B921692H>.

[67] Q. Gu, J. Long, L. Fan, L. Chen, L. Zhao, H. Lin, X. Wang, Single-site Sn-grafted Ru/TiO₂ photocatalysts for biomass reforming: synergistic effect of dual co-catalysts and molecular mechanism, *J. Catal.* 303 (2013) 141–155, <https://doi.org/10.1016/j.jcat.2013.03.014>.

[68] C. Clavero, Plasmon-induced hot-electron generation at nanoparticle/metal-oxide interfaces for photovoltaic and photocatalytic devices, *Nat. Photonics* 8 (2014) 95–103, <https://doi.org/10.1038/nphoton.2013.238>.

[69] K. Wu, J. Chen, J.R. McBride, T. Lian, Efficient hot-electron transfer by a plasmon-induced interfacial charge-transfer transition, *Science* 349 (2015) 632–634, <https://doi.org/10.1126/science.aac5443>.

[70] K. Wu, W.E. Rodríguez-Córdoba, Y. Yang, T. Lian, Plasmon-induced hot electron transfer from the Au tip to CdS Rod in CdS–Au nanoheterostructures, *Nano Lett.* 13 (2013) 5255–5263, <https://doi.org/10.1021/nl402730m>.

[71] G. Liu, P. Li, G. Zhao, X. Wang, J. Kong, H. Liu, H. Zhang, K. Chang, X. Meng, T. Kako, J. Ye, Promoting active species generation by plasmon-induced hot-electron excitation for efficient electrocatalytic oxygen evolution, *J. Am. Chem. Soc.* 138 (2016) 9128–9136, <https://doi.org/10.1021/jacs.6b05190>.

[72] X. Ma, Y. Dai, L. Yu, B. Huang, New basic insights into the low hot Electron injection efficiency of gold-nanoparticle–photosensitized titanium dioxide, *ACS Appl. Mater. Interfaces* 6 (2014) 12388–12394, <https://doi.org/10.1021/am502251j>.

[73] D.C. Ratchford, A.D. Dunkelberger, I. Vurgaftman, J.C. Owrutsky, P.E. Pehrsson, Quantification of efficient plasmonic hot-electron injection in gold nanoparticle–TiO₂ films, *Nano Lett.* 17 (2017) 6047–6055, <https://doi.org/10.1021/acs.nanolett.7b02366>.

[74] W. Hou, S.B. Cronin, A review of surface plasmon resonance-enhanced photocatalysis, *Adv. Funct. Mater.* 23 (2013) 1612–1619, <https://doi.org/10.1002/adfm.201202148>.

[75] S.K. Cushing, J. Li, F. Meng, T.R. Senty, S. Suri, M. Zhi, M. Li, A.D. Bristow, N. Wu, Photocatalytic activity enhanced by plasmonic resonant energy transfer from metal to semiconductor, *J. Am. Chem. Soc.* 134 (2012) 15033–15041, <https://doi.org/10.1021/ja305603t>.

[76] J. Li, S.K. Cushing, P. Zheng, T. Senty, F. Meng, A.D. Bristow, A. Manivannan, N. Wu, Solar hydrogen generation by a CdS–Au–TiO₂ sandwich nanorod array enhanced with Au nanoparticle as electron relay and plasmonic photosensitizer, *J. Am. Chem. Soc.* 136 (2014) 8438–8449, <https://doi.org/10.1021/ja503508g>.

[77] C. Xue, G.S. Métraux, J.E. Millstone, C.A. Mirkin, Mechanistic study of photo-mediated triangular silver nanoprisms growth, *J. Am. Chem. Soc.* 130 (2008) 8337–8344, <https://doi.org/10.1021/ja8005258>.

[78] C. Xue, J.E. Millstone, S. Li, C.A. Mirkin, Plasmon-driven synthesis of triangular core–shell nanoprisms from gold seeds, *Angew. Chem. Int. Ed.* 46 (2007) 8436–8439, <https://doi.org/10.1002/anie.200703185>.

[79] R.P. Wang, G. Xu, P. Jin, Size dependence of electron–phonon coupling in ZnO nanowires, *Phys. Rev. B* 69 (2004) 113303, <https://doi.org/10.1103/PhysRevB.69.113303>.

[80] H.M. Cheng, K.F. Lin, H.C. Hsu, W.F. Hsieh, Size dependence of photoluminescence and resonant Raman scattering from ZnO quantum dots, *Appl. Phys. Lett.* 88 (2006) 261909, <https://doi.org/10.1063/1.2217925>.

[81] A.K. Ojha, M. Srivastava, S. Kumar, R. Hassanein, J. Singh, M.K. Singh, A. Materny, Influence of crystal size on the electron–phonon coupling in ZnO nanocrystals investigated by Raman spectroscopy, *Vib. Spectrosc.* 72 (2014) 90–96, <https://doi.org/10.1016/j.vibspec.2014.02.013>.